

Decadal Variability in a Simplified Wind-Driven Ocean Model

PHILIP SURA, FRANK LUNKEIT, AND KLAUS FRAEDRICH

Meteorologisches Institut, Universität Hamburg, Hamburg, Germany

(Manuscript received 30 October 1998, in final form 3 September 1999)

ABSTRACT

The impact of an unsteady wind forcing on oceanic low-frequency variability is conceptually studied using a reduced-gravity shallow-water model. A time-averaged wind forcing and a simple ocean–atmosphere coupling is completed by a stochastic component (spatially coherent white noise) representing the effect of atmospheric transient eddies. To account for the observed concentration of eddy activity along the North Atlantic and North Pacific storm tracks the variance of the stochastic forcing is chosen to be spatially inhomogeneous. Low-frequency variability of the basin-averaged energetics shows a dominant spectral peak with an amplitude depending on the inhomogeneity of the stochastic forcing and the time-averaged wind stress. The period of the variability is unexpected considering baroclinic Rossby waves forced by the ocean–atmosphere coupling only. This variability can be explained by “spatial resonance” of the forced baroclinic Rossby wave and the Reynolds momentum flux induced by the spatially inhomogeneous white noise.

1. Introduction

The climate of the earth exhibits natural variability on timescales ranging from years to centuries of which the decadal variability, with periods between approximately 5 and 50 years, is attracting more and more interest. Its dynamics has to be understood before interpreting man-made climate variations. In recent years several observational studies focusing on decadal timescales have been published. Deser and Blackmon (1993) analyzed data from the Comprehensive Ocean–Atmosphere Data Set (COADS) and find decadal climate variations over the North Atlantic Ocean. They suggest that surface wind anomalies contribute to the formation of sea surface temperature (SST) anomalies by altering the fluxes of latent and sensible heat at the ocean surface. Kushnir (1994), analyzing observed data of the North Atlantic region, suggests that there exists a strong coupling between SST anomalies and the atmospheric circulation. Levitus et al. (1994) investigate ocean temperature records from Ocean Weather Station C (52.75°N, 35.5°W). Hurrell (1995) identifies a decadal period of the North Atlantic oscillation (NAO) index. A drawback of observational datasets is their short duration. Therefore, coupled and uncoupled oceanic and atmospheric general circulation models are used to study possible mechanisms of long-term climate variability.

Several hypotheses have been put forward to explain climate variability on decadal timescales. Due to the large density and heat capacity, the oceans seem to play a key role in determining the period of decadal climate variability with two distinct contributors: the thermohaline and the wind-driven circulation. This study focuses on the role of the wind-driven circulation, although it is accepted that the thermohaline circulation plays an important part in producing decadal climate variability (Greatbatch and Zhang 1995; Saravanan and McWilliams 1997; Weaver and Sarachik 1991; Winton and Sarachik 1993). Three mechanisms are suggested to explain fluctuation on decadal timescales due to the wind-driven circulation: stochastically forced variability, variability driven by coupled ocean–atmosphere dynamics, and fluctuations arising from the inherent nonlinear behavior of the wind-forced circulation.

The *stochastic scenario* is based on the Brownian motion analog (Hasselmann 1976). The observed red spectrum of oceanic fluctuations is a consequence of the amplification of low-frequency weather fluctuations. In this concept decadal variability is the low-frequency part of the red oceanic spectrum. Frankignoul and Müller (1979) investigate the response of a stratified quasigeostrophic ocean on an infinite β plane to stochastic wind forcing; the baroclinic part of the model simulates a red frequency spectrum. Frankignoul et al. (1997) introduce more realistic boundaries by an eastern coast and a radiation condition in the west. They identify the baroclinic response to a stochastic wind forcing by a red frequency spectrum with a dominant period, determined by the time for a nondispersive baroclinic Rossby wave

Corresponding author address: Dr. Frank Lunkeit, Meteorologisches Institut der Universität Hamburg, Bundesstraße 55, D-20146 Hamburg, Germany.
E-mail: lunkeit@dkrz.de

to cross the entire basin. This period increases with the basin width.

The *coupled ocean–atmosphere scenario* (Bjerknes 1964) connects long-term SST variability with changing heat transports of wind-driven ocean currents. Latif and Barnett (1994, 1996) using a coupled atmospheric–oceanic general circulation model (AOGCM) found a decadal climate cycle over the North Pacific that involves the subtropical gyre and the Aleutian low; anomalous warm water transported northward by the Kuroshio leads to positive SST anomalies in the North Pacific weakening the Aleutian low. The weakened Aleutian low produces a wind-stress curl anomaly that reduces the subtropical gyre and, thus, the heat transport in the western boundary current (Kuroshio). The net effect is a reduced SST anomaly in the North Pacific. After all, the North Pacific climate system oscillates on a decadal timescale. The same mechanism is proposed for the North Atlantic climate system (Grötzner et al. 1998) using a coupled AOGCM. For both regions the period of the oscillation is approximately the time a nondispersive free baroclinic Rossby wave needs to cross the North Pacific or North Atlantic basin. Precisely, the oceanic response in the coupled ocean–atmosphere scenario is a wave that propagates with a phase speed twice that of the free Rossby wave, as indicated by simplified models (Jin 1997; Münnich et al. 1998; Weng and Neelin 1998). Nevertheless, it is not clear that the coupled ocean–atmosphere scenario is a viable mechanism for explaining midlatitude climate variability. Therefore, simplified models can assist in studying the role of ocean–atmosphere interactions.

Variability of the wind-driven circulation induced by the *nonlinear scenario* is investigated by Jiang et al. (1995) and McCalpin and Haidvogel (1996) using a reduced-gravity double-gyre model in a rectangular basin. Modulated by the chosen parameters the free jet (as the conceptual analog to the Gulf Stream) becomes unstable and oscillates with a decadal period between two available states.

The present study explores both the *stochastic scenario* and the *coupled ocean–atmosphere scenario*, utilizing a reduced-gravity model to study the low-frequency variability of the classical rectangular basin. The reduced-gravity approximation is considered to be the simplest conceptual representation of the real ocean; it includes Rossby wave dynamics and shear-flow instabilities. In a simplified manner, the atmosphere provides the mean wind stress, the stochastic input, and the ocean–atmosphere coupling.

A double-gyre configuration is used to represent the mean wind field. The stochastic forcing generates atmospheric weather fluctuations by spatially coherent white noise, whose variance is chosen to be spatially inhomogeneous. This stochastic component is introduced to parameterize the localized variability of the midlatitude atmospheric dynamics, whose intense synoptic-scale activity is related to storm tracks following

the jet stream axes. The ocean–atmosphere coupling is reduced to a nonlocal interaction between wind and thermocline depth anomalies. Here, the amplitude of the wind stress is assumed to depend on the local thermocline perturbation in a given index region (Münnich et al. 1998).

The primary objective of the paper is to investigate the effect of the spatially inhomogeneous stochastic wind stress on the variability of the ocean circulation. In section 2 the reduced-gravity model, the wind stress forcing, and the corresponding numerical scheme are described. Section 3 presents the experimental design and the results of the numerical experiments. Section 4 gives a physical explanation of a decadal mode. Finally, section 5 provides a summary and a discussion of the results.

2. Ocean model and atmospheric forcing

a. Ocean model

The nonlinear reduced-gravity equations in transport form are used to model the upper ocean in a rectangular basin of 3600 km by 3600 km extent representing the North Atlantic region; (x, y) coordinates increasing eastward and northward are used. In the reduced-gravity approximation the ocean is represented by a single active layer of constant density ρ_1 of thickness H . The upper layer is assumed to overlie a deep and motionless layer of density ρ_2 . With this constraint only the first baroclinic mode is modeled. That is, the interface between the two layers represents the permanent thermocline. The eastward and northward transport is defined as $U = uH$ and $V = vH$, whereby u and v are the corresponding velocities, τ^x and τ^y are the wind stress components, g is the acceleration of gravity, and f is the Coriolis parameter given by the β -plane approximation, $f = f_0 + \beta y$. Thus, the equations are

$$\frac{\partial U}{\partial t} + \frac{\partial}{\partial x} \left(\frac{U^2}{H} \right) + \frac{\partial}{\partial y} \left(\frac{UV}{H} \right) - fV = \frac{-g'}{2} \frac{\partial H^2}{\partial x} + \frac{\tau^x}{\rho_1} - rU + A\Delta U \quad (1)$$

$$\frac{\partial V}{\partial t} + \frac{\partial}{\partial x} \left(\frac{UV}{H} \right) + \frac{\partial}{\partial y} \left(\frac{V^2}{H} \right) + fU = \frac{-g'}{2} \frac{\partial H^2}{\partial y} + \frac{\tau^y}{\rho_1} - rV + A\Delta V \quad (2)$$

$$\frac{\partial H}{\partial t} + \frac{\partial U}{\partial x} + \frac{\partial V}{\partial y} = 0, \quad (3)$$

where the reduced gravity is $g' = g(\rho_2 - \rho_1)/\rho_2$.

Interfacial friction is parameterized by Rayleigh friction scaled by r ; the lateral viscosity is represented by a Laplacian scaled by A . All parameters of the model are summarized in Table 1. For dynamical parameters standard numerical values are used. The Laplacian friction coefficient is chosen to adjust the width of the Munk

TABLE 1. Model parameters.

Coriolis parameter	$f = 1.03 \times 10^{-4} \text{ s}^{-1}$
Beta effect	$\beta = 1.62 \times 10^{-11} \text{ m}^{-1} \text{ s}^{-1}$
Upper-layer equilibrium depth	$H_0 = 500 \text{ m}$
Rayleigh friction coefficient	$r = 1 \times 10^{-7} \text{ s}^{-1}$
Laplacian friction coefficient	$A = 2 \times 10^3 \text{ m}^2 \text{ s}^{-1}$
Upper-layer density	$\rho_1 = 1027 \text{ kg m}^{-3}$
Lower-layer density	$\rho_2 = 1030 \text{ kg m}^{-3}$
Reduced gravity	$g' = 0.029 \text{ m s}^{-2}$
Wind stress amplitude	$\tau_0 = 0.05 \text{ N m}^{-2}$
Time step	$\Delta t = 1 \text{ h}$
Domain extent (north–south)	$L_y = 3600 \text{ km}$
Domain extent (east–west)	$L_x = 3600 \text{ km}$
Grid resolution	$\Delta x = 50 \text{ km}$ $\Delta y = 50 \text{ km}$

layer $\delta_M = (A/\beta)^{1/3}$ to approximately the width of the numerical grid.

The equations of motion are solved numerically on a staggered Arakawa C grid. The model resolution is 50 km in both the zonal and meridional direction. The choice of the coarse resolution, as compared to eddy resolving models with resolutions of 10–20 km, is justified by the aim to understand the results of long-term (several centuries) climate simulations. At present it is not possible to run a complex AOGCM with an eddy-resolving ocean component. To interpret the results of complex AOGCMs it is therefore necessary to use simplified models with a comparable resolution to separate specific physical mechanisms. Nevertheless, it is expected that the grid size of 50 km is fine enough to resolve the eddy momentum fluxes induced by the stochastic wind forcing to be at least qualitatively correct. This is justified by the fact that the oceanic response to a stochastic wind stress is dominated by length scales much larger than the Rossby radius (Frankignoul and Müller 1979). The Rossby radius in the model used is approximately 40–80 km. Furthermore, Frankignoul and Müller expect that stochastic forcing by the wind is a dominant generating mechanism for eddies only in the central part of the oceans because eddy generation by instabilities occurs mainly in the vicinity of intense boundary currents. Therefore, it appears reasonable to use a model with a resolution of 50 km to study effects of the stochastic wind forcing, bearing in mind that highly inertial boundary currents and the corresponding instabilities are not resolved with this resolution.

Time differencing is performed by the Matsuno (Euler backward) scheme, space differencing by space-centered finite difference approximations. The nonlinear advection terms are computed by first averaging the prognostic variables in space to calculate the required products at the appropriate mesh points before the centered finite differences are calculated. The no-flux boundary condition is used to suppress the normal flow at the boundaries. Furthermore, a half-slip condition is employed. The choice of the half-slip condition is due to Haidvogel et al. (1992), who suggest that the tangential

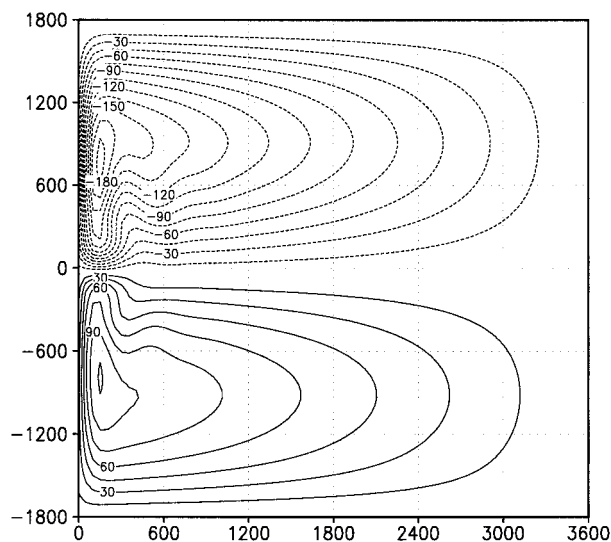


FIG. 1. Steady-state interface depth anomaly h (m) for the mean double-gyre wind forcing: $\tau = \tau_{\text{mean}}$. The axes are horizontal distances in kilometers.

velocities at the boundaries should lie between the no-slip and the free-slip limits.

Two standard definitions are introduced that are used throughout the rest of the paper. The layer thickness H is the sum of the equilibrium depth H_0 and the depth anomaly h so that $H(x, y, t) = H_0 + h(x, y, t)$. Furthermore, all time-dependent variables ψ are separated into a long-term mean $\bar{\psi}$ and a deviation ψ' , $\psi = \bar{\psi} + \psi'$.

b. Atmospheric forcing

The atmospheric forcing of the ocean by the wind stress consists of a mean field, a stochastic field, and a large-scale ocean–atmosphere coupling

$$\tau = \tau_{\text{mean}} + \tau_{\text{stochastic}} + \tau_{\text{coupled}}. \quad (4)$$

The mean wind stress τ_{mean} is represented by a zonal wind field of a sinusoidal pattern

$$\tau_{\text{mean}}^x = \tau_0 \cos\left(\frac{2\pi y}{L_y}\right), \quad -\frac{L_y}{2} \leq y \leq \frac{L_y}{2}. \quad (5)$$

This generates a northern cyclonic subpolar and a southern anticyclonic subtropical gyre. The wind stress amplitude τ_0 is set to a standard value of 0.05 N m^{-2} . The steady interface anomaly h due to the mean wind stress is shown in Fig. 1. The solution is in a slightly nonlinear regime as can be seen by the weak recirculation gyres at the western boundary.

The spatially inhomogeneous stochastic forcing $\tau_{\text{stochastic}}$ accounts for the atmospheric noise and is parameterized by the bulk formula for the wind stress. The bulk formula is preferred to the direct use of the wind stress components as it renders it possible to preserve the eddy kinetic energy of the atmosphere in all exper-

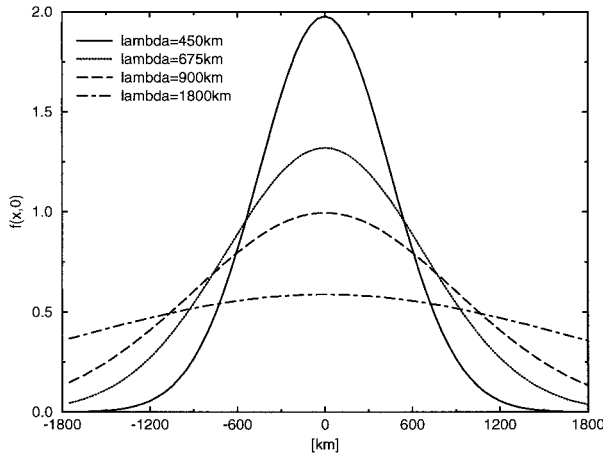


FIG. 2. The shape of the weight function $f(x, y)$ for different values of the inhomogeneity parameter λ at $y = 0$. The choice of the scaling constant α is described in the text.

iments. This leads to the parameterization of the spatially inhomogeneous stochastic forcing

$$\begin{aligned}\tau_{\text{stochastic}} &= \rho_{\text{air}} C_D |\mathbf{u}'| \mathbf{u}' \\ u'(x, y, t) &= \alpha \eta_x(t) f(x, y) \\ v'(x, y, t) &= \alpha \eta_y(t) f(x, y),\end{aligned}\quad (6)$$

where ρ_{air} , $|\mathbf{u}'|$, and \mathbf{u}' are the air density (1.3 kg m^{-3}), near-surface wind speed, and velocity; C_D (2×10^{-3}) is the drag coefficient, α is a scaling constant, and $\eta_{x,y}(t)$ is white noise with zero mean and standard deviation σ . In the numerical integration the white noise is updated once a day. The weight function $f(x, y)$ parameterizes the spatial structure of the atmospheric variability by a Gaussian shape, whose origin is placed in the center of the basin

$$f(x, y) = C \exp\left(-\frac{x^2}{2\lambda_x^2} - \frac{y^2}{2\lambda_y^2}\right). \quad (7)$$

Here C normalizes the area integral of the squared weight function over the basin domain Ω to unity: $C = [\pi\lambda_x\lambda_y \text{erf}(L_x/2\lambda_x) \text{erf}(L_y/2\lambda_y)]^{-1/2}$ with the error function erf . The inhomogeneity parameters, λ_x and λ_y , control the spatial structure of the atmospheric variability. To obtain circular symmetry of the stochastic forcing, $\lambda_x = \lambda_y = \lambda$. A Gaussian shape with circular symmetry is chosen for convenience to parameterize the localized atmospheric eddy activity along the storm tracks in a conceptual manner. This parameterization is justified by the observed horizontal structure of wind-speed standard deviations [see, e.g., the COADS data prepared by Wright (1988)]. The shapes associated with different λ values used in the subsequent numerical experiments are shown in Fig. 2. The scaling constant α is chosen to adjust the weight function in the origin to 1 for $\lambda = 900 \text{ km}$. The variance σ^2 of the white noise is $28 \text{ m}^2 \text{ s}^{-2}$, characterizing the observed atmospheric conditions

in the North Atlantic region. That is, for intermediate inhomogeneity parameters ($\lambda = 675$ and 900 km) the variance of the wind speed in the center of the basin is approximately between 28 and $42 \text{ m}^2 \text{ s}^{-2}$, and is therefore comparable to observed conditions (Wright 1988).

The large-scale ocean–atmosphere coupling procedure is represented by τ_{coupled} . The atmosphere is reduced to an instantaneous nonlocal wind-stress feedback to thermocline depth anomalies (Münnich et al. 1998). The amplitude of the wind stress anomalies depends on the thermocline perturbation $h'(t)$ in a suitable index region Γ . The spatial pattern of the anomalies remains unchanged. For simplicity a sinusoidal anomaly pattern is used

$$\tau_{\text{coupled}} = -\mu[h'(t)]_{\Gamma} \sin\left(\frac{\pi y}{L_y}\right), \quad -\frac{L_y}{2} \leq y \leq \frac{L_y}{2}, \quad (8)$$

with horizontal averaging over the index region Γ denoted by brackets; μ is a coupling constant set to 0.05 N m^{-3} . The index region Γ is a square of 500-km length at the western boundary of the basin at $x = 0$ and $y = 0$ to capture the feedback mechanism due to the northward heat transport by the western boundary current. The choice of the index region is conceptually comparable to the feedback mechanism used in the simplified model of Weng and Neelin (1998). In contrast to the present study, Weng and Neelin use a model that has an explicit SST equation. Nevertheless, their projection of the actual SST on a fixed SST basis pattern parameterizes the ocean–atmosphere interaction through the use of fixed spatial wind-stress and heat-flux feedback patterns. Because the SST basis pattern and the heat flux pattern are localized at the western boundary of the basin, their feedback mechanism is conceptually comparable to the simplified coupling through thermocline depth anomalies at the western boundary. Münnich et al. (1998) show that such a simple coupling produces decadal oscillations that are comparable to the results of Weng and Neelin (1998) and that the oscillations are rather insensitive to the coupling strength. Furthermore, the patterns of oceanic variability are even similar to those observed in the North Pacific if a realistic wind stress anomaly pattern is used. For this reason it is plausible to use the simple coupling procedure as a conceptual tool to study midlatitude atmosphere–ocean interactions, keeping in mind that the detailed atmospheric response to SST anomalies is far from being well understood.

The typical time evolution of the spatial pattern driven by the simple coupling procedure is shown by a sequence of depth anomalies h (Fig. 3). The sequence is computed by initializing the model with a broad depth anomaly in the center of the basin. A positive anomaly with an anticyclonic circulation reaches the western boundary at year 31 and $[h'(t)]_{\Gamma}$ becomes positive. Therefore, the wind stress anomalies are changing their sign, forcing a cyclonic gyre with a negative depth

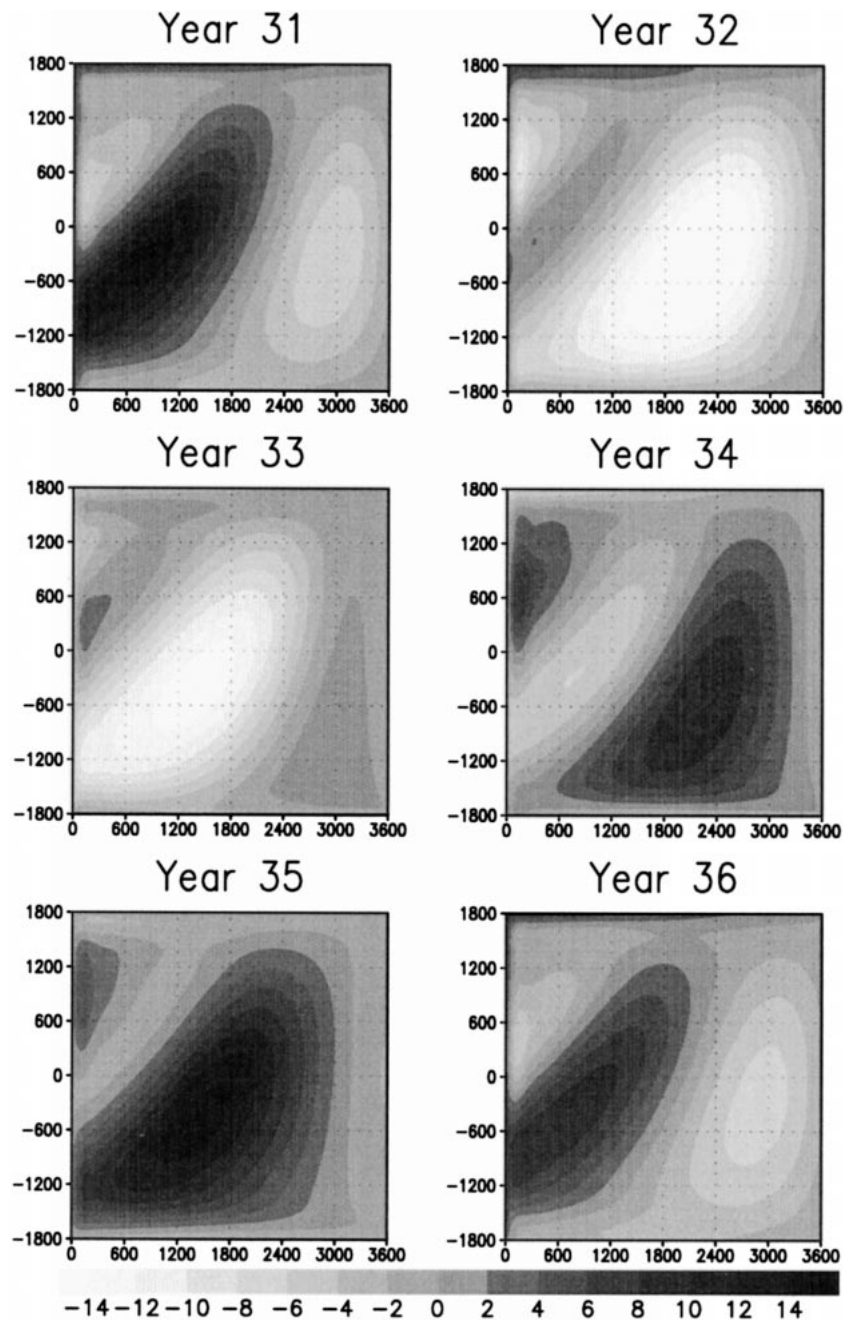


FIG. 3. Snapshots of the depth anomalies h (m) for a coupled wind stress scenario: $\tau = \tau_{\text{coupled}}$. The axes are horizontal distances in kilometers.

anomaly h that is seen in year 32. The negative anomaly reaches the western boundary between year 33 and 34. That is, a phase reversal is attained after 2.5 years, allowing the system to oscillate with a period of about 5 yr. The anomalies propagate to the west with twice the zonal phase speed of a free nondispersive Rossby wave, $C_x = -\beta R^2$ with the internal Rossby radius $R = (g'H_0)^{1/2}/f = C_0/f$. The southern fronts of the anomalies are bent to the west due to higher Rossby wave speeds

in lower latitudes. It is well known that, in a simplified model driven by a zonally uniform but time-dependent wind forcing, the wave travels with a speed that is twice the free wave speed (White 1977; Frankignoul et al. 1997). Thus, the period of about 5 yr is twice the time a forced Rossby wave needs to cross the entire basin from east to west, where they finally excite the feedback.

For the subsequent discussion it is important to note that the coupling manifests itself with a period of 5 yr

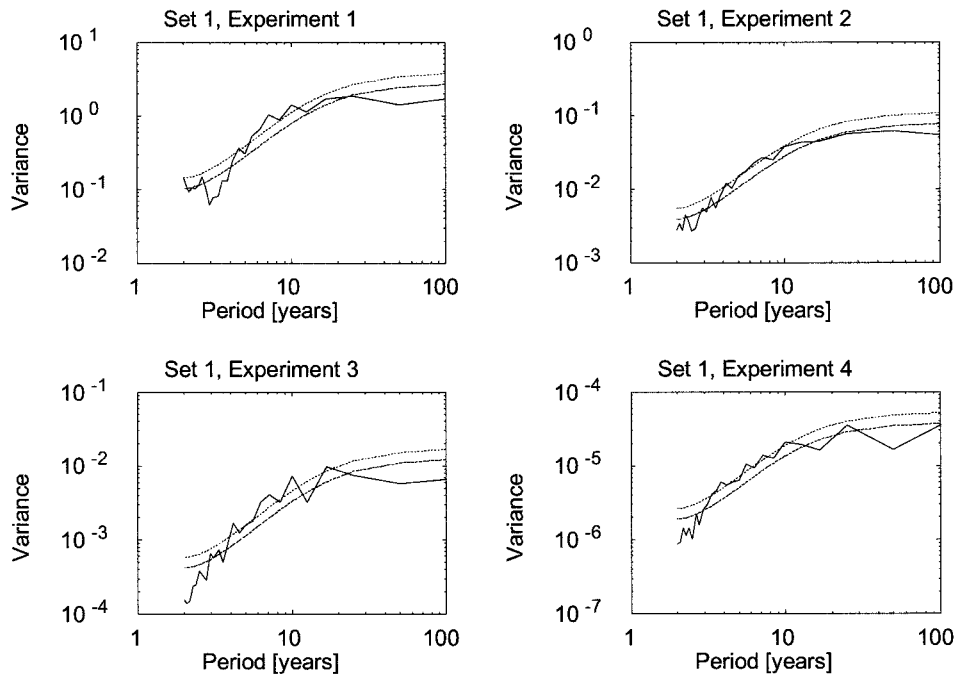


FIG. 4. Variance spectra ($J^2 \text{ yr m}^{-4}$) of eddy kinetic energies for set 1 ($\tau = \tau_{\text{stochastic}}$). The equivalent AR(1) process is indicated by a dashed line; the 95% confidence limit is indicated by a dotted line.

in quantities like the depth anomaly, the velocity, or the transport. It would appear as a 2.5-yr period in the corresponding energy time series, because the 5-yr coupling period halves through the use of squared quantities.

3. Numerical experiments: Design and results

a. Experimental design

The effect of the spatially inhomogeneous stochastic wind stress on the ocean circulation in the uncoupled and coupled mode is analyzed by four sets of experiments. Each set consists of four experiments (1, . . . , 4) defined by the inhomogeneity parameter $\lambda = 450, 675, 900,$ and 1800 km . In set 1, the mean wind stress and the coupling are neglected ($\tau_1 = \tau_{\text{stochastic}}$); in set 2 the coupling procedure is performed, still ignoring the mean wind stress ($\tau_2 = \tau_{\text{stochastic}} + \tau_{\text{coupled}}$). Sets 3 and 4 correspond to the previous sets, with the exception that the double-gyre wind stress is included: $\tau_3 = \tau_{\text{mean}} + \tau_{\text{stochastic}}$ and $\tau_4 = \tau_{\text{mean}} + \tau_{\text{stochastic}} + \tau_{\text{coupled}}$.

The experiments of sets 1 and 2 are started from a resting state while the experiments of sets 3 and 4 commence from the mean double-gyre state; all experiments are integrated for 1000 years. Transports, velocities, and depth anomalies are saved once a day. For all further diagnostics annual means are used to calculate the basin-integrated eddy kinetic energies and conversion terms (see below) because it is reasonable to employ the period of the nondispersive first baroclinic Rossby mode in midlatitudes as an appropriate timescale, which has the order of years.

b. Experimental results

A convenient overall description of the transient behavior of the basin circulation can be given in terms of the integrated eddy kinetic energy content in the entire basin domain Ω . The basin-integrated eddy kinetic energy is defined by

$$[E'_{\text{kin}}]_{\Omega} = \frac{1}{\Omega} \iint_{\Omega} \left(\frac{\rho_1 \bar{H}}{2} (u'^2 + v'^2) \right) dx dy. \quad (9)$$

Horizontal averaging over the entire basin domain Ω is denoted by brackets. Henceforth, the term eddy kinetic energy is used for $[E'_{\text{kin}}]_{\Omega}$, if not stated otherwise.

The transient behavior of the basin circulation is characterized by the variance spectra of the time series of the eddy kinetic energies. The spectra of the equivalent first-order autoregressive AR(1) processes, estimated from the respective time series, and the 95% confidence limits for accepting the red noise null hypothesis are also computed. The spectra are obtained from the 1000-yr time series of the annual means of the eddy kinetic energies. The data are split up into 20 segments of 50 years so that the longest resolvable period is 25 yr. Eddy kinetic energy time series based on monthly means do not change the basic results of this section.

Set 1 ($\tau_1 = \tau_{\text{stochastic}}$): Figure 4 shows the spectra of the eddy kinetic energy time series of all four experiments. A red noise behavior on the decadal timescale is observed as expected from the stochastic climate scenario. Increasing the inhomogeneity, that is, decreasing the parameter λ , does not lead to changes in the qual-

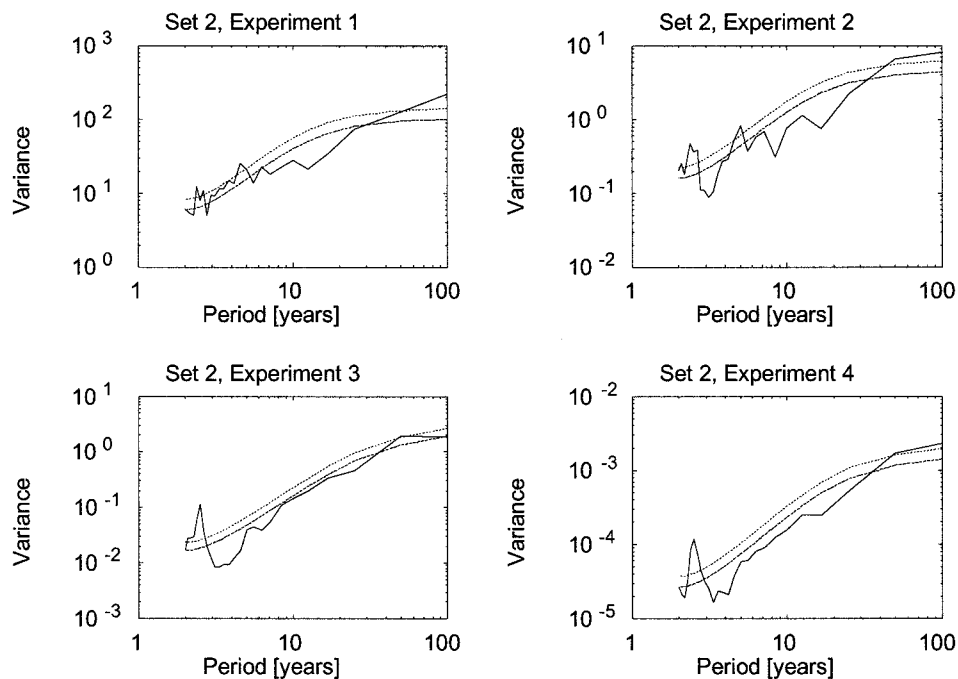


FIG. 5. Variance spectra ($\text{J}^2 \text{ yr m}^{-4}$) of eddy kinetic energies for set 2 ($\tau = \tau_{\text{stochastic}} + \tau_{\text{coupled}}$). The equivalent AR(1) process is indicated by a dashed line; the 95% confidence limit is indicated by a dotted line.

itative structure of the spectra; it merely enhances the overall variance of the transient motion because the wind stress curl of the stochastic forcing driving the large-scale ocean circulation decreases with increasing λ . That is, the eddy kinetic energy and the corresponding variance depends strongly on the spatially inhomogeneous structure of the stochastic forcing.

Set 2 ($\tau_2 = \tau_{\text{stochastic}} + \tau_{\text{coupled}}$): The eddy kinetic energy spectra for all experiments of set 2 (Fig. 5) also show red noise. But, at a period of 2.5 yr all spectra exhibit a peak significant at the 95% level above the red noise background. It is essential to recognize that this period is induced by the coupling procedure because energy is used for diagnostics. That is, the 5-yr coupling period appears as a 2.5-yr peak in the eddy kinetic energy spectra through the use of squared velocities, as discussed previously. In contrast to all experiments of set 1, there is now an unexpected significant signal due to the spatially inhomogeneous structure of the stochastic forcing. As long as the stochastic forcing is nearly spatially homogeneous (expt 4 with $\lambda = 1800$ km) only the 2.5-yr coupling peak is significant. Increasing the inhomogeneity, that is, if the parameter λ is decreased to 900 km (expt 3), a small spectral peak appears at a period of 5 yr, which, however, is not yet significant. Further enhancement of the spatial inhomogeneity (expt 2 with $\lambda = 675$ km) shows that the 5-yr peak becomes significant above the 95% confidence limit so that the spectrum exhibits two significant peaks with periods of 2.5 and 5 yr above the red noise background. This effect

is slightly diminished if λ is decreased further to 450 km (expt 1). Another remarkable feature is that the 2.5-yr coupling peak becomes less pronounced as the parameter λ is decreased from 1800 to 450 km. This effect is due to the enhanced variance of the transient motion driven by the noise because the wind stress curl of the stochastic forcing decreases with increasing λ . Thus, the 2.5-yr coupling peak is “hidden” by the variance induced by the stochastic forcing.

Set 3 ($\tau_3 = \tau_{\text{mean}} + \tau_{\text{stochastic}}$): The spectra for all experiments of set 3 (not shown) are essentially red and similar to set 1. The only feature is the higher overall variance compared to the zero mean forcing case of set 1. This effect is due to the instabilities of the mean circulation.

Set 4 ($\tau_4 = \tau_{\text{mean}} + \tau_{\text{stochastic}} + \tau_{\text{coupled}}$): Including the mean circulation dampens the spectra of set 4 (Fig. 6) as compared to the experiments of set 2. The coupling peak is less pronounced and shifted to a slightly higher period of approximately 3 yr. As in set 2, experiment 2 of set 4 ($\lambda = 675$ km) exhibits enhanced variability at a period of approximately two times the coupling period. This period of about 6 yr, however, is not significant above the 95% confidence limit.

4. The mechanism of a decadal mode

In the previous section it has been shown that there exists a mechanism that produces an unexpected significant spectral peak with a period of about 5 yr in the

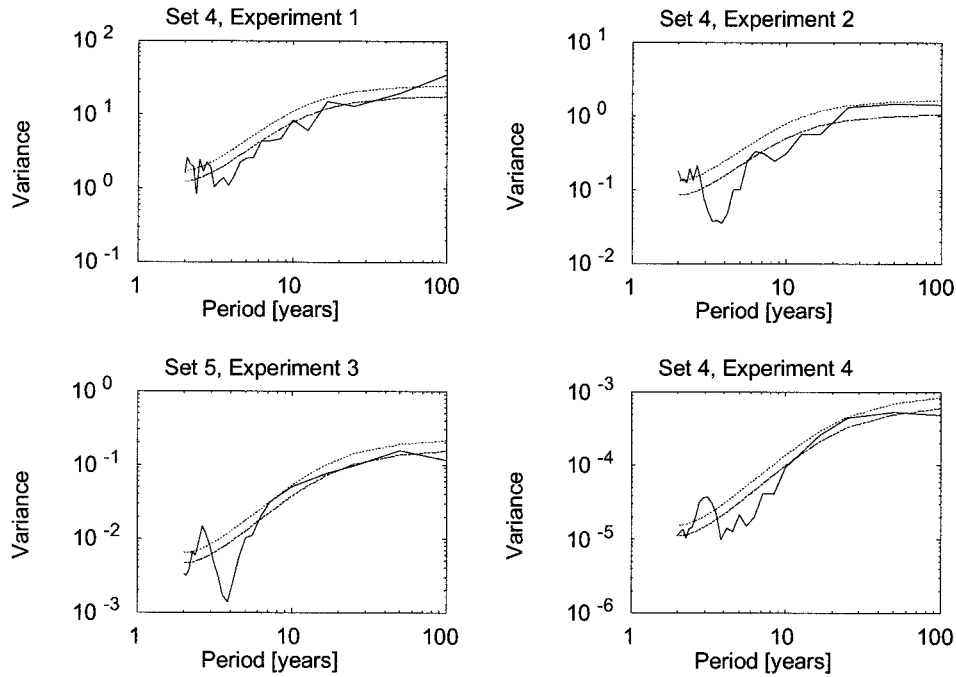


FIG. 6. Variance spectra ($\text{J}^2 \text{ yr m}^{-4}$) of eddy kinetic energies for set 4 ($\tau = \tau_{\text{mean}} + \tau_{\text{stochastic}} + \tau_{\text{coupled}}$). The equivalent AR(1) process is indicated by a dashed line; the 95% confidence limit is indicated by a dotted line.

spectra of the basin-integrated eddy kinetic energy time series. The most pronounced spectral peak appears in the simplified coupling case with spatially inhomogeneous stochastic forcing and zero mean wind stress (set 2). The basic mechanism of the mode under consideration is explained first, neglecting its damping by the mean wind forcing.

a. Energetics

The eddy kinetic energy budget is used for interpretation of the mechanism that drives the 5-yr mode in the eddy kinetic energy time series (see the appendix). The basin averages of the conversion terms of (A6) provide a convenient overall description of the oscillatory behavior of the system. The following energy conversion terms that do not contribute to an oscillatory behavior of the basin are excluded. The advection of eddy kinetic energy vanishes when integrated over a closed domain. The conversion between mean and eddy kinetic energy is neglectable because, in the experiments of set 1 and set 2, the mean circulation is weak (but not zero, as shown later). The term describing the geostrophic adjustment process is not able to account for the oscillatory behavior of the system because the wind-driven circulation is nearly in quasigeostrophic balance. Therefore, the term is a sink for the eddy kinetic energy. The same holds for the dissipative terms because they are energy sinks. The wind stress in the simplified cou-

pling scenario drives the oscillatory motion of the 2.5-yr peak, but does not account for a periodic behavior of another significant timescale. The stochastic component of the wind stress drives the smooth red spectrum of the eddy motion (Hasselmann 1976). Examining their signs and the spectra, the conversion terms described above can be excluded as generating mechanisms.

Only the Reynolds term

$$u' \left(\frac{\partial \overline{u'^2}}{\partial x} + \frac{\partial \overline{u'v'}}{\partial y} \right) + v' \left(\frac{\partial \overline{u'v'}}{\partial x} + \frac{\partial \overline{v'^2}}{\partial y} \right) \quad (10)$$

is able to generate the observed 5-yr peak in the eddy energy spectra. In Fig. 7, the cross-spectrum of the time series of the basin-integrated eddy kinetic energy and the basin-integrated Reynolds term of experiment 2 of set 2 are displayed. Both time series are normalized to a unit standard deviation because the magnitudes of both time series are very different. On the 99% confidence level they are coherent at the period of 5 yr, where the Reynolds term is leading the time series of the eddy kinetic energy with a phase of about 100 deg or 1.4 yr.

b. Dynamics

The mechanism of the unexpected 5-yr variability in the eddy kinetic energy time series requires explanation facing three facts.

- The period is about twice the time the forced Rossby

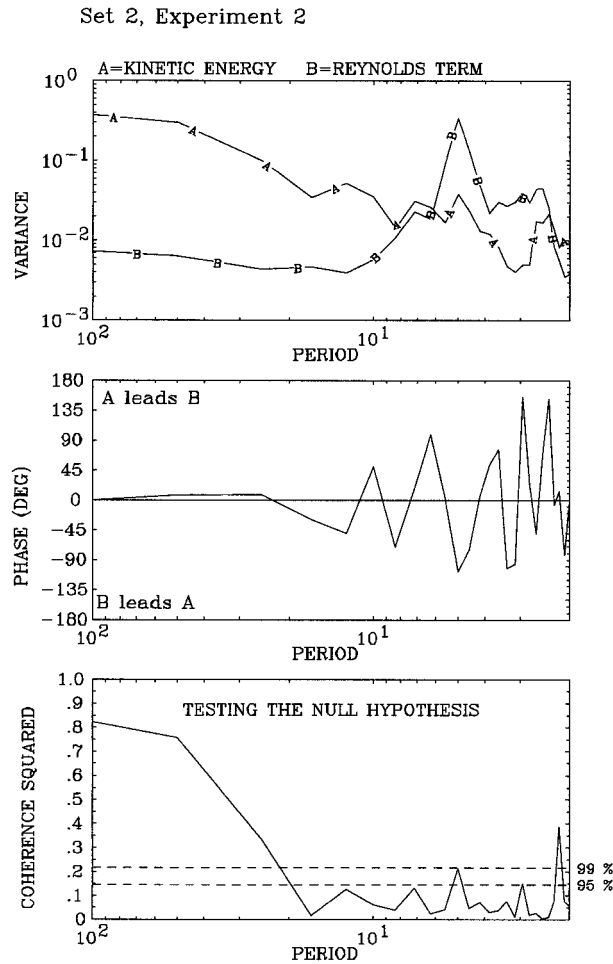


FIG. 7. Normalized variance spectra (yr), phase spectrum, and coherence spectrum of the basin-integrated eddy kinetic energy and the basin-integrated Reynolds term for expt 2 of set 2. The period is in years. Both time series are normalized to a unit standard deviation.

waves (driven, e.g., by the coupling scenario) need to cross the entire basin from east to west.

- The Rossby wave dynamics is connected with an energy flux induced by the Reynolds term.
- The 5-yr oscillation in the eddy energy time series depends sensitively on the spatial structure of the atmospheric white noise forcing controlled by the inhomogeneity parameter λ of the weight function $f(x, y)$. An optimal forcing is achieved for a relatively strong spatial inhomogeneity; for values above and below $\lambda = 675$ km the forcing is diminished.

It is important to note that the 5-yr variability in the eddy kinetic energy time series is not a basin mode of the quasigeostrophic potential vorticity equation. The eigenfrequencies in the reduced-gravity case are too high to account for the observed 5-yr variability. Even higher harmonics of the eigenfrequencies have a period of only 2 yr. In fact, all first baroclinic basin modes

resolved by the resolution used have approximately the same frequency $\omega_{mn} = (\beta R)/(2\pi)$. Furthermore, the 5-yr oscillation is not a higher eigenmode of the coupled ocean–atmosphere system. Münnich et al. (1998), Jin (1997), and Weng and Neelin (1998) show that, even with spatially inhomogeneous stochastic wind forcing, their linear coupled models do not show other coupled modes than the one described in section 2. Thus, the 5-yr variability is indeed connected with the energy flux induced by the Reynolds term, which does not appear in linear ocean models.

The following mechanism is proposed, guided by the schematic illustration presented in Fig. 8, where the three columns represent (a) the spatially inhomogeneous stochastic forcing, (b) the coupled ocean–atmosphere scenario, and (c) spatial resonance.

The *spatially inhomogeneous stochastic forcing* (Fig. 8a), which drives oceanic eddies, is indicated by the line widths in the upper box representing the atmosphere. These oceanic eddies, however, induce a cyclonic Reynolds momentum flux due to their inhomogeneous spatial distribution, as described below. Holland (1978) examined the fundamental role of the interaction of the oceanic eddy field with the mean state. The present paper examines the interaction of the oceanic eddy field with the eddies itself. Recognize that the Reynolds momentum fluxes appear with opposite signs in the momentum equations describing the mean circulation [(A1) and (A2)] and the eddy momentum balance [(A3) and (A4)]. The dashed line in the lower box (representing the ocean) shows the idealized structure and the direction of the Reynolds momentum flux induced by the eddies. Note that the Reynolds momentum fluxes are stationary per definition (see the appendix). For this reason these fluxes cause a steady cyclonic forcing in the eddy momentum balance [(A3) and (A4)]. The spatial inhomogeneity of the oceanic eddies is a manifestation of the oceanic response to the inhomogeneous stochastic forcing by the atmosphere. Now, the direction of the momentum flux in the ocean can be easily deduced in polar coordinates. They account for the nearly circular symmetry of the problem, although the actual horizontal pattern of the Reynolds momentum flux does not show a perfect circular symmetry. The circular pattern is distorted by the westward propagation of the eddies, but, in the conceptual framework used, it is appropriate to assume circular symmetry for convenience. The basic physical mechanisms are not affected by that conceptual assumption. If u_θ and u_r are the tangential and radial velocity components, the rate of change of the tangential component of the transient field due to the Reynolds stresses is governed by

$$\frac{\partial u'_\theta}{\partial t} \propto \frac{\partial \overline{u'_\theta u'_r}}{\partial r}. \quad (11)$$

As indicated by the numerical experiments the velocity correlations decrease radially outward. This decrease is

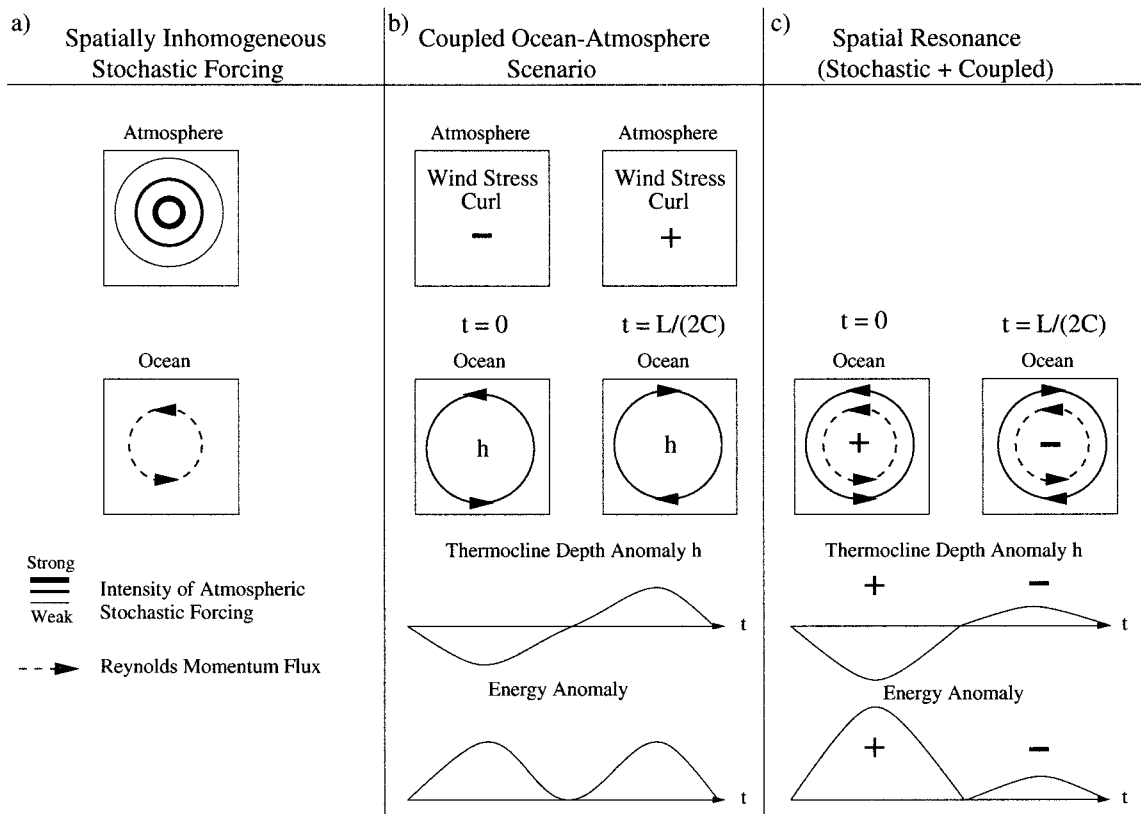


FIG. 8. Schematic illustration of the proposed mechanism. See the text for a detailed description. (a) The *spatially inhomogeneous stochastic forcing*: In the upper box (representing the atmosphere) the line width illustrates the intensity of the stochastic forcing. In the lower box (representing the ocean) the dashed line shows the structure and the direction of the Reynolds momentum flux. (b) The *coupled ocean-atmosphere scenario*: The upper panel shows the sign of the wind stress curl. The solid lines in the middle panel show the structure and the phase of the Rossby wave traveling to the west. Here, L is the zonal basin width and C is the magnitude of the zonal phase speed of a free nondispersive Rossby wave. Schematic time series of thermocline depth anomalies and the corresponding energy anomalies are illustrated at the bottom of the column. (c) *Spatial resonance*: The ocean boxes illustrate the interaction between the Reynolds momentum flux and the Rossby wave. Plus/minus signs denote the phase of Rossby wave-Reynolds momentum flux interaction. The resulting time series are shown at the bottom of the column.

due to the Gaussian shape of the atmospheric stochastic forcing, which has the maximum variance in the center of the basin and decreases radially outward. Therefore, the radial gradient of the velocity correlations in (11) is negative, creating a momentum flux in the cyclonic direction. As the spatial inhomogeneity of the stochastic forcing becomes stronger, the corresponding spatial gradients of the Reynolds stresses in the momentum equations increase gradually; thus, the momentum flux is enhanced. To verify this in Cartesian coordinates, south-north profiles of the velocity correlations $\overline{u'v'}$ and $\overline{v'v'}$ at $x = 1800$ km are presented in Fig. 9 for experiment 2 of sets 1 and 2; that is, the inhomogeneity parameter $\lambda = 675$ km yields the optimal forcing. Both sets reveal a pronounced Gaussian shape of the velocity correlations (in set 2 the structure is only slightly distorted). If the stochastic forcing is chosen to be nearly homogeneous, the velocity correlations become almost con-

stant within the basin, and the corresponding momentum fluxes vanish (not shown).

The *coupled ocean-atmosphere scenario* (Fig. 8b) forces large-scale Rossby waves, as discussed previously. To recapitulate, a negative thermocline depth anomaly with a cyclonic circulation implies a negative wind stress curl anomaly due to the feedback mechanism at $t = 0$. The anomaly propagates to the west with twice the zonal phase speed of a free nondispersive Rossby wave, $C_x = -\beta R^2$. Therefore, a phase reversal is attained after the Rossby wave crossing time

$$t = L_x / (2\beta R^2)$$

of about 2.5 yr, which allows the system to oscillate with a period two times the Rossby wave crossing time, $T = L_x / (\beta R^2)$, of about 5 years. As before, circular symmetry is assumed in Fig. 8 for convenience. The actual patterns are shown in Fig. 3. Note that the cou-

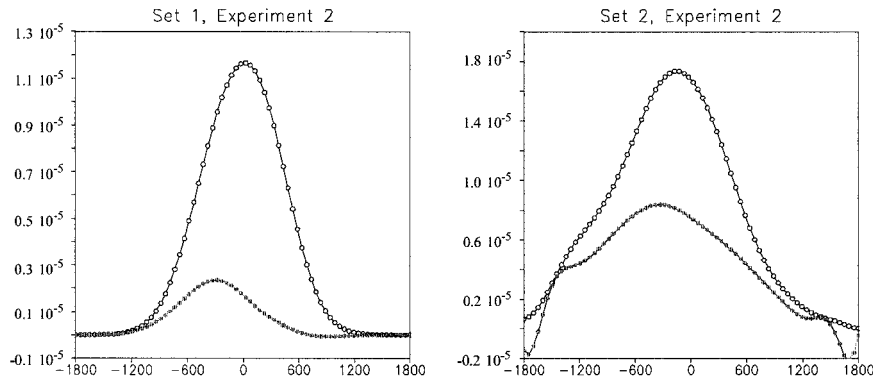


FIG. 9. South–north profile of velocity correlations ($\text{m}^2 \text{s}^{-2}$) at $x = 1800 \text{ km}$: $\overline{v'v'}$ is indicated by a circle and $\overline{u'v'}$ by a full circle. The abscissa is the south–north distance in kilometers.

pling period $T = L_x/(\beta R^2)$ appears as $T/2 = L_x/(2\beta R^2)$ in the energy anomalies, as indicated by the schematic time series.

Spatial resonance becomes possible, if the spatially inhomogeneous stochastic forcing and the coupled ocean–atmosphere scenario coexist (Fig. 8c). The Rossby wave interacts in a spatially resonant manner with the Reynolds momentum flux; that is, the optimal forcing is achieved if the spatial pattern of the Reynolds momentum fluxes induced by the stochastic forcing fits best to the structure of the Rossby wave pattern forced by the simplified coupling procedure. In this case of spatial resonance the amplitude of the Rossby wave is optimally amplified and, in the reverse phase, diminished through the momentum flux induced by the Reynolds stresses. The time interval between an amplified and the next diminished phase is approximately 2.5 yr.

Therefore, the time interval between two amplified phases, as well as between two diminished phases, is about 5 years. Note that, although the cyclonic eddy momentum flux is stationary, the Reynolds term in the eddy energy equation (10) changes its sign periodically because of the Rossby wave forced by the coupling procedure. At $t = 0$ the Rossby wave pattern, which is traveling westward with twice the free wave speed, is optimally excited by the Reynolds momentum fluxes induced by the spatially inhomogeneous stochastic forcing, denoted by a plus sign in Fig. 8c. In that phase energy is put into the system. At phase reversal, attained after the crossing time $t = L_x/(2\beta R^2)$ of about 2.5 years, the amplitude of the wave is diminished, denoted by a minus sign. Thus, energy is drained out of the system. After 5 years, the phase of the system occurs again, which is optimally excited by the inhomogeneous stochastic forcing. The resulting time series of the thermocline depth anomalies is shown schematically. Note that in the corresponding energy time series a period of $T = L_x/(\beta R^2)$ (about 5 yr) appears due to the use of squared quantities. For this reason a peak at the 5-yr period is observed in the basin-integrated eddy energy. The term “spatial resonance” is adopted from Saravanan and McWilliams (1997), denoting the response of a system at its preferred spatial pattern.

Because the amplitude of the Rossby wave is amplified in the cyclonic phase and diminished in the anticyclonic phase, the mode does not vanish in the time-averaged circulation. That means, if the schematic time series of the thermocline depth anomaly in the case of spatial resonance is integrated in time, the result would be positive. In fact, in the case of spatial resonance the amplified phase of the Rossby wave manifests itself in the mean circulation. In Fig. 10 the mean interface depth anomaly h for the experiment with the optimal forcing (set 2 with $\lambda = 675 \text{ km}$) is shown. The structure equals that of the Rossby wave pattern (see Fig. 3). None of the other experiments of set 2 show this. If the stochastic

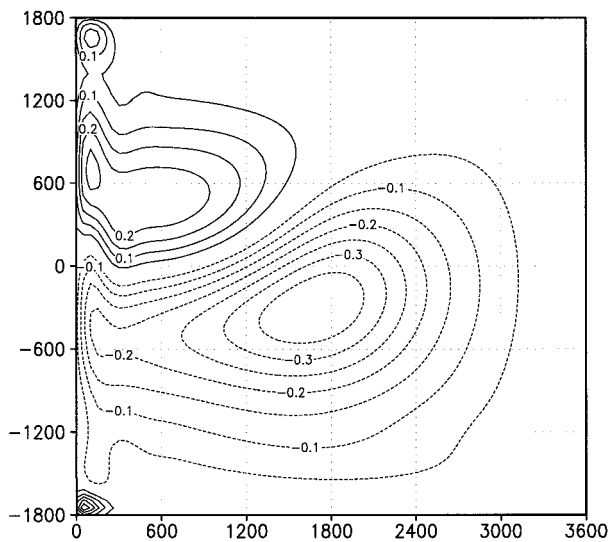


FIG. 10. Mean interface depth anomaly h (m) for expt 2 of set 2. The axes are horizontal distances in kilometers.

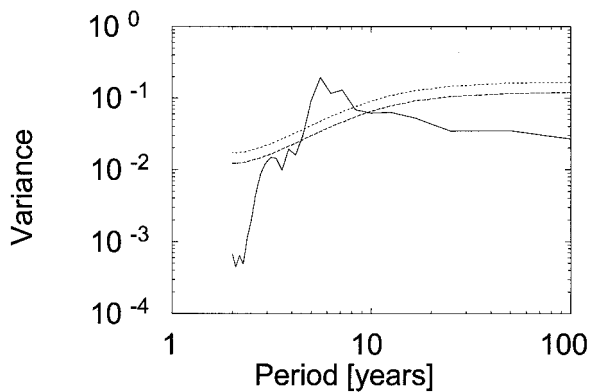


FIG. 11. Normalized variance spectra (yr) of the basin-integrated Reynolds conversion term for expt 2 of set 4 ($\tau = \tau_{\text{mean}} + \tau_{\text{stochastic}} + \tau_{\text{coupled}}$). The equivalent AR(1) process is indicated by a dashed line; the 95% confidence limit is indicated by a dotted line. The time series is normalized to a unit standard deviation.

forcing is chosen to be almost spatially homogeneous, there is no considerable mean circulation at all.

Examining the sign of the Reynolds term in more detail, it is seen that the phase in Fig. 10 is indeed the forced phase of the Rossby wave. Considering only the south–north profiles of the meridional gradients of the correlations and the zonal velocity u' at $x = 1800$ (neglecting v'), only $u'(\partial u'v'/\partial y)$ contributes to the Reynolds term. The sign of this term is always positive for the amplified phase of the oscillation: North of $y = -300$ km, u' and $\partial u'v'/\partial y$ are both negative; south of $y = -300$ km, u' and $\partial u'v'/\partial y$ are both positive. Just the opposite is true for the diminished phase of the oscillation.

Finally, the damping of the 5-yr mode by the mean wind forcing remains to be discussed. The spatial structure of the time-averaged velocity correlations shows that the eddy field driven by the stochastic forcing is not distorted significantly by the advective effect of the mean double-gyre circulation. The same holds for the forced Rossby wave driven by the coupling procedure. The reason is that only baroclinic Rossby waves with wavelengths smaller than a few hundred kilometers are noticeably influenced by the mean currents. This length scale is, however, not predominantly generated by the stochastic forcing. Hence, the spatial resonance mechanism is still at work in the presence of the mean wind stress, as realized in the spectrum of the Reynolds conversion term of experiment 2 of set 4 (Fig. 11). For this reason, the spatial resonance mechanism is damped by another superimposed effect. This is probably the conversion between mean and eddy kinetic energy because the eddy field is not distorted significantly by the mean circulation, except in the boundary layer region.

Because the main focus of the paper is to investigate possible physical mechanisms of decadal variability in simplified coupled models, the damping of the spatial resonance mechanism by the mean wind stress is not

subject of a detailed analysis in the present paper. Indeed, the exclusion of the mean circulation is common in conceptual models to separate possible mechanisms of ocean–atmosphere feedbacks. The role of the discussed mechanism in more complex models deserves further research.

5. Summary and discussion

A simple ocean model is used to explore its low-frequency variability driven by an unsteady wind forcing. The wind stress consists of a mean field, a stochastic field, and an ocean–atmosphere coupling. The amplitude of the Rossby wave driven by the coupling procedure is significantly amplified and, in the reverse phase, diminished if the spatially inhomogeneous stochastic forcing fits best with the Rossby mode structure. For this reason a peak at a period of 5 yr is observed in the basin-integrated eddy energy content. In this case of spatial resonance the Rossby wave is optimally forced by the Reynolds momentum fluxes induced by the spatially inhomogeneous stochastic forcing of the atmosphere, which accounts for the observed concentration of eddy activity along the storm tracks.

Thus, decadal climate variability induced by the *coupled ocean–atmosphere scenario* (Bjerknes 1964; Latif and Barnett 1994, 1996; Grötzner et al. 1998; Jin 1997; Münnich et al. 1998; Weng and Neelin 1998) can be substantially modified by the *stochastic scenario* (Hasselmann 1976; Frankignoul and Müller 1979; Frankignoul et al. 1997). It has to be stressed that the conceptual framework of the postulated mechanism allows its application to other basin dimensions, yielding other significant periods, as long as the spatially inhomogeneous stochastic forcing is present, which induces the Reynolds momentum flux. Furthermore, the Rossby wave interacting in a spatially resonant manner with the Reynolds momentum fluxes could be generated by mechanisms other than the ocean–atmosphere coupling; the source of the Rossby wave is not an inherent feature of the resonance mechanism. That is, every Rossby-like basin mode could be modified by the spatially inhomogeneous stochastic forcing of the atmosphere in the case of spatial resonance.

A comparable mechanism of spatial resonance has been suggested by Saravanan and McWilliams (1997) in the context of the thermohaline circulation using an idealized coupled atmosphere–ocean model to investigate the ocean–atmosphere interaction on an interdecadal timescale. Their model exhibits interdecadal oscillations of the thermohaline circulation with a preferred timescale of 30–40 yr. The half-period of the mode appears to be related to the mid- to high-latitude advection time of SST anomalies (Greatbatch and Zhang 1995; Weaver and Sarachik 1991). The interesting feature is the excitation of the thermohaline mode. Saravanan and McWilliams assume that there exist one or more normal modes of the ocean with preferred spatial

SST patterns and preferred timescales. Under this assumption those oceanic modes with surface patterns that most closely match the preferred atmospheric spatial patterns will be the ones most efficiently excited. This kind of spatial resonance appears to be responsible for the oceanic interdecadal oscillation.

In this sense, the mechanism of the mode described in the present paper is comparable to that proposed by Saravanan and McWilliams (1997). The oceanic component is not the thermohaline mode, but the Rossby wave driven by the coupling procedure; this Rossby mode is then modified by the momentum flux induced by the spatially inhomogeneous structure of the stochastic wind stress forcing, which contrasts the spatial structure of the low-frequency heat-flux forcing pattern. In both cases the spatial resonance between an oceanic mode and an atmospheric forcing pattern is responsible for modifying or exciting an oceanic mode.

Although the model used in the present paper is very simple, the postulated mechanism is expected to be a useful concept for the excitation of oceanic low-frequency variability.

Acknowledgments. This work was supported by the Deutsche Forschungsgemeinschaft within Sonderforschungsbereich 512. We thank the two anonymous reviewers for their valuable comments that led to improvements of the original manuscript.

APPENDIX

The Energy Equations

In this appendix the equations governing the eddy kinetic energy budget are derived and discussed briefly.

Applying the conventional temporal averaging operator to the reduced-gravity momentum equations in the conventional velocity form it follows that

$$\begin{aligned} \bar{u} \frac{\partial \bar{u}}{\partial x} + \frac{\partial \bar{u}'^2}{\partial x} + \bar{v} \frac{\partial \bar{u}}{\partial y} + \frac{\partial \bar{u}'v'}{\partial y} - f\bar{v} \\ = -g' \frac{\partial \bar{H}}{\partial x} + \frac{\bar{\tau}_x}{\rho_1 \bar{H}} + A \nabla^2 \bar{u} - r\bar{u} \end{aligned} \quad (\text{A1})$$

$$\begin{aligned} \bar{u} \frac{\partial \bar{v}}{\partial x} + \frac{\partial \bar{u}'v'}{\partial x} + \bar{v} \frac{\partial \bar{v}}{\partial y} + \frac{\partial \bar{v}'^2}{\partial y} + f\bar{u} \\ = -g' \frac{\partial \bar{H}}{\partial y} + \frac{\bar{\tau}_y}{\rho_1 \bar{H}} + A \nabla^2 \bar{v} - r\bar{v}, \end{aligned} \quad (\text{A2})$$

whereby it is assumed that the eddy fields are in quasi-geostrophic balance and $\bar{H} \gg H'$. Subtracting the equations from the reduced-gravity momentum equations gives the eddy momentum balance

$$\begin{aligned} \frac{\partial u'}{\partial t} + (\bar{u} + u') \frac{\partial u'}{\partial x} + (\bar{v} + v') \frac{\partial u'}{\partial y} + u' \frac{\partial \bar{u}}{\partial x} + v' \frac{\partial \bar{u}}{\partial y} - f v' \\ = -g' \frac{\partial H'}{\partial x} + \frac{\tau'_x}{\rho_1 \bar{H}} + A \nabla^2 u' - r u' + \frac{\partial \bar{u}'^2}{\partial x} + \frac{\partial \bar{u}'v'}{\partial y} \end{aligned} \quad (\text{A3})$$

$$\begin{aligned} \frac{\partial v'}{\partial t} + (\bar{u} + u') \frac{\partial v'}{\partial x} + (\bar{v} + v') \frac{\partial v'}{\partial y} + u' \frac{\partial \bar{v}}{\partial x} + v' \frac{\partial \bar{v}}{\partial y} + f u' \\ = -g' \frac{\partial H'}{\partial y} + \frac{\tau'_y}{\rho_1 \bar{H}} + A \nabla^2 v' - r v' + \frac{\partial \bar{u}'v'}{\partial x} + \frac{\partial \bar{v}'^2}{\partial y}. \end{aligned} \quad (\text{A4})$$

In order to derive the energy equation, (A3) and (A4) are multiplied by u' and v' . Adding the resulting equations and defining the eddy kinetic energy per unit mass as

$$EM'_{\text{kin}} = \frac{1}{2}(u'^2 + v'^2) = \frac{E'_{\text{kin}}}{\rho_1 \bar{H}} \quad (\text{A5})$$

gives the equation describing the temporal change of the eddy kinetic energy

$$\begin{aligned} \frac{\partial EM'_{\text{kin}}}{\partial t} = & - \left(\bar{u} \frac{\partial EM'_{\text{kin}}}{\partial x} + \bar{v} \frac{\partial EM'_{\text{kin}}}{\partial y} + u' \frac{\partial EM'_{\text{kin}}}{\partial x} + v' \frac{\partial EM'_{\text{kin}}}{\partial y} \right) \\ & - \left(u'^2 \frac{\partial \bar{u}}{\partial x} + u'v' \frac{\partial \bar{u}}{\partial y} + u'v' \frac{\partial \bar{v}}{\partial x} + v'^2 \frac{\partial \bar{v}}{\partial y} \right) \\ & - g' \left(u' \frac{\partial H'}{\partial x} + v' \frac{\partial H'}{\partial y} \right) + A(u' \nabla^2 u' + v' \nabla^2 v') \\ & + \frac{(u' \tau'_x + v' \tau'_y)}{\rho_1 \bar{H}} - r(u'^2 + v'^2) \\ & + u' \left(\frac{\partial \bar{u}'^2}{\partial x} + \frac{\partial \bar{u}'v'}{\partial y} \right) + v' \left(\frac{\partial \bar{u}'v'}{\partial x} + \frac{\partial \bar{v}'^2}{\partial y} \right). \end{aligned} \quad (\text{A6})$$

The local rate of change of the eddy kinetic energy is balanced by several processes. The first term on the right-hand side of (A6) represents the advection of eddy kinetic energy by the mean and the transient velocity field; the second term is associated with the conversion between mean and eddy kinetic energy. The third term accounts for the conversion between eddy kinetic and eddy potential energy, normally designated as the geostrophic adjustment process. The following three terms describe the energy conversions due to the transient wind stress and the dissipative processes. The last two terms of (A6) are essential in the present paper; they represent the eddy energy conversion induced by the momentum flux of the velocities fluctuations. This term appears as a result of averaging each momentum equation and is henceforth called the Reynolds term. Note that the Reynolds term vanishes after temporal aver-

aging; that is, the energy budget for time mean eddy kinetic energy $\overline{EM'_{kin}}$ is not affected by the Reynolds term.

REFERENCES

- Bjerknes, J., 1964: Atlantic air–sea interaction. *Advances in Geophysics*, Vol. 10, Academic Press, 1–82.
- Deser, C., and M. L. Blackmon, 1993: Surface climate variations over the North Atlantic Ocean during winter: 1900–1989. *J. Climate*, **6**, 1743–1753.
- Frankignoul, C., and P. Müller, 1979: Quasi-geostrophic response of an infinite β -plane ocean to stochastic forcing by the atmosphere. *J. Phys. Oceanogr.*, **9**, 104–127.
- , —, and E. Zorita, 1997: A simple model of the decadal response of the ocean to stochastic wind forcing. *J. Phys. Oceanogr.*, **27**, 1533–1546.
- Greatbatch, R. J., and S. Zhang, 1995: An interdecadal oscillation in an idealized ocean basin forced by constant heat flux. *J. Climate*, **8**, 81–91.
- Grötzner, A., M. Latif, and T. P. Barnett, 1998: A decadal climate cycle in the North Atlantic Ocean as simulated by the ECHO coupled GCM. *J. Climate*, **11**, 831–847.
- Haidvogel, D. B., J. C. McWilliams, and P. R. Gent, 1992: Boundary current separation in a quasigeostrophic, eddy-resolving ocean circulation model. *J. Phys. Oceanogr.*, **22**, 882–902.
- Hasselmann, K., 1976: Stochastic climate models. Part I. Theory. *Tellus*, **28**, 473–484.
- Holland, W. R., 1978: The role of mesoscale eddies in the general circulation of the ocean—Numerical experiments using a wind-driven quasi-geostrophic model. *J. Phys. Oceanogr.*, **8**, 363–392.
- Hurrell, J. W., 1995: Decadal trends in the North Atlantic Oscillation: Regional temperatures and precipitation. *Science*, **269**, 676–679.
- Jiang, S., F.-F. Jin, and M. Ghil, 1995: Multiple equilibria, periodic, and aperiodic solutions in a wind-driven, double-gyre, shallow-water model. *J. Phys. Oceanogr.*, **25**, 764–786.
- Jin, F.-F., 1997: A theory of interdecadal climate variability of the North Pacific ocean–atmosphere system. *J. Climate*, **10**, 1821–1835.
- Kushnir, Y., 1994: Interdecadal variations in North Atlantic sea surface temperature and associated atmospheric conditions. *J. Climate*, **7**, 141–157.
- Latif, M., and T. B. Barnett, 1994: Causes of decadal climate variability over the North Pacific and North America. *Science*, **266**, 634–637.
- , and —, 1996: Decadal climate variability over the North Pacific and North America: Dynamics and predictability. *J. Climate*, **9**, 2407–2423.
- Levitus, S., J. I. Antonov, and T. P. Boyer, 1994: Interannual variability of temperature at a depth of 125 m in the North Atlantic Ocean. *Science*, **266**, 96–99.
- McCalpin, J., and D. B. Haidvogel, 1996: Phenomenology of the low-frequency variability in a reduced-gravity quasigeostrophic double-gyre model. *J. Phys. Oceanogr.*, **26**, 739–752.
- Münnich, M., M. Latif, S. Venske, and E. Maier-Reimer, 1998: Decadal oscillations in a simple coupled model. *J. Climate*, **11**, 3309–3319.
- Saravanan, R., and J. C. McWilliams, 1997: Stochasticity and spatial resonance in interdecadal climate fluctuations. *J. Climate*, **10**, 2299–2320.
- Weaver, A. J., and E. S. Sarachik, 1991: Evidence for decadal variability in an ocean general circulation model: An advective mechanism. *Atmos.–Ocean*, **29**, 197–231.
- Weng, W., and J. D. Neelin, 1998: On the role of ocean–atmosphere interaction in midlatitude interdecadal variability. *Geophys. Res. Lett.*, **25**, 167–170.
- White, W. B., 1977: Annual forcing of baroclinic long waves in the tropical North Pacific Ocean. *J. Phys. Oceanogr.*, **7**, 50–61.
- Winton, M., and E. S. Sarachik, 1993: Thermohaline oscillations induced by strong steady salinity forcing of ocean general circulation models. *J. Phys. Oceanogr.*, **23**, 1713–1724.
- Wright, P. B., 1988: An atlas based on the COADS data set: Fields of mean wind, cloudiness and humidity at the surface of the global ocean. Max-Planck-Institut für Meteorologie Rep. No. 14, 68 pp. [Available from Max-Planck-Institut für Meteorologie, Bundesstrasse 55, D-20146 Hamburg, Germany.]